Reducing ice adhesion on non-smooth metallic surfaces: wettability and topography effects

Edwin Jee Yang Ling

Victor Uong

Jean-Sébastien Renault-Crispo

Anne-Marie Kietzig

*Phillip Servio**

Department of Chemical Engineering, McGill University, 3610 University Street, Montréal, Québec, H3A 0C5, Canada.

*Corresponding author: +1 (514) 398-1026; phillip.servio@mcgill.ca

Keywords:

Ice adhesion

Surface wettability

Surface topography

Mechanical interlocking

Stress concentrations

Crack propagation

This is the accepted manuscript of Ling*, EJY; Uong, V; Renault-Crispo, JS; Kietzig, AM; Servio, P. (2016). Reducing ice adhesion on nonsmooth metallic surfaces: wettability and topography effects. ACS Applied Materials & Interfaces. 8(13): 8789-8800. https://doi.org/10.1021/acsami.6b00187

Abstract

The effects of ice formation and accretion on external surfaces range from being mildly annoying to potentially life-threatening. Ice-shedding materials, which lower the adhesion strength of ice to its surface, have recently received renewed research attention as a means to circumvent the problem of icing. In this work, we investigate how surface wettability and surface topography influence the ice adhesion strength on three different surfaces: i) superhydrophobic laser-inscribed square pillars on copper, ii) stainless steel 316 Dutch-weaved meshes, and iii) multi-walled carbon nanotube (MWCNT)-covered steel meshes. The finest stainless steel mesh displayed the best performance with a 93% decrease in ice adhesion relative to polished stainless steel, while the superhydrophobic square pillars exhibited an increase in ice adhesion by up to 67% relative to polished copper. Comparison of dynamic contact angles revealed little correlation between surface wettability and ice adhesion. On the other hand, by considering the ice formation process and the fracture mechanics at the ice-substrate interface, we found that two competing mechanisms governing ice adhesion strength arise on non-planar surfaces: i) mechanical interlocking of the ice within the surface features that enhances adhesion, and ii) formation of micro-cracks that act as interfacial stress concentrators, which reduce adhesion. Our analysis provides insight towards new approaches for the design of ice-releasing materials through the use of surface topographies that promote interfacial crack propagation.

1. Introduction

Ice formation on exterior surfaces has been a persistent nuisance and hazard for outdoor infrastructure such as offshore platforms,[1] asphalt roads and pavements,[2] power transmission lines,[3] aircraft parts (engines, wings, and tail),[4] wind turbines,[5] solar panels,[6] helicopter blades,[7] and even space shuttle components.[8] While ice removal is typically accomplished via active de-icing techniques (thermal, mechanical, and/or chemical) that require continued reapplication,[9] recent advances in surface technologies have ushered in the development of so-called "ice-phobic" materials, whose interfacial properties either prevent ice formation or reduce its adhesion, or both.[3] The first approach – preventing ice formation – may be achieved by either fabricating non-wetting surfaces that repel impinging water droplets such that the surface remains dry,[10-13] or by designing surfaces that delay ice nucleation.[12, 14-16] The second approach involves lowering the adhesion strength of ice to a surface, allowing for easy ice removal. Both approaches have been implemented by altering the chemical properties of the surface (polymeric coatings,[9, 17-19] self-assembled monolayers,[20] etc.) and/or modifying its topography (photolithography,[21] laser surface texturing,[22-23] anodization,[24] etc.). Menini et al.,[9] Boinovich and Emelanenko,[25] and Schutzius et al.[26] have recently published reviews, each providing a comprehensive treatment on different aspects of anti-icing.

Designing a surface that successfully incorporates both approaches – in addition to meeting end-use-specific requirements of robustness, affordability, installation, and maintenance – has proven to be an exceptionally challenging task. The main difficulty stems from the fact that, in order to render a surface superhydrophobic, it must be furnished with micro- and nano-scale surface structures that resist inter-feature water penetration.[27] Varanasi et al.[28] showed that under cold and humid conditions, frost formation between surface asperities resulted in a Cassie-to-Wenzel wetting transition, which, in turn, led to a significant increase in ice adhesion strength. Furthermore, numerous studies have shown that when liquid water freezes on a superhydrophobic surface exhibiting micro- and nano-scale roughness, the tips of the surface asperities become incorporated within the ice due to its volume expansion during freezing.[13, 20, 29-31] Subsequent ice removal fractures and damages these surface structures, compromising the performance of these non-wetting surfaces. This, along with the added fact that these structures are generally mechanically fragile, begs the question of whether water-repellent surfaces are really the best candidates for anti-icing applications in harsh environmental conditions.

The alternative is, as mentioned before, to design surfaces on which ice may form but weakly adheres to; these are also known as ice-shedding or ice-releasing materials. Table 1 presents a list, albeit an incomplete one, of the recent advances towards developing surfaces that exhibit low ice adhesion. From here, we see that there are primarily three strategies employed to achieve lowered ice adhesion: i) coating the base material with a compound containing low surface energy components in order to render the surface more hydrophobic,[17-19, 31-32] ii) introducing micro- and nano-scale structures to the surface, which, when combined with a hydrophobic coating, have the ability to render the surface superhydrophobic,[21, 31-32] and iii) using coatings infused with an organic[16, 33-34] or aqueous[35] liquid that acts as a lubricating layer. The greatest reduction in ice adhesion is obtained by the latter strategy, which boasts an adhesion reduction factor (*ARF*) of up to 87.2,[16] where $ARF = \tau_{control}/\tau_{ice}$ and τ_{ice} is the ice adhesion stress.

Table 1. Review of recent advances in developing ice-shedding materials. This list is by no means complete but serves to demonstrate key highlights from literature. R_a, θ, θ_A, θ_R, τ_{ice}, and *ARF* refer to the surface roughness (arithmetic mean of absolute values), sessile water contact angle, advancing contact angle, receding contact angle, ice adhesion stress, and adhesion reduction factor = $\tau_{control}/\tau_{ice}$, respectively.

Report	Surface treatment	R_a (μm)	θ or θ_A/θ_R (°)[b]	τ_{ice} (kPa)	*ARF*[d]
Bharathidasan et al.[19]	Room temperature vulcanized (RTV) silicone rubber coating	0.38	105	24.8 ± 8	43.2
	RTV silicone rubber coating with fumed silica particles	4.46	158	243 ± 20	4.4
Davis et al.[32]	Spray-casted polyurethane/silica/fluoroacrylic coating on Al	2.7	159/144	680	2.5
		8.7	159/152	1430	1.2
Dou et al.[35]	Polyurethane-based aqueous lubricating layer on Al, but also possible on ceramics and polymers	–	66[c]	27	30.3
Farhadi et al.[31]	Etched Al coated with fluoroalkyl silane	≤ 0.32[a]	166	~65	~7
He et al.[21]	Micro/nano-pillars on Si	–	148/147	420 ± 20	4.8[e]
Kim et al.[16]	Slippery, liquid-infused porous surfaces (SLIPS)	–	117/115	15.6 ± 3.6	87.2
Meuler et al.[17]	80/20 PEMA/fluorodecyl POSS spin coated on steel	0.9 ± 0.2	124/118	165 ± 27	4.2[f]
Susoff et al.[18]	Sol-gel containing Fluorolink® on bare Al	0.24	~120	~60	~20
	Sol-gel containing Fluorolink® on sandblasted Al	0.59	–	~700	~2
Zhu et al.[33]	Cross-linked PDMS infused with silicone oil ~30 wt% and silica particles on Al	0.00858	121	~40	30

a: The value reported was for R_q (root-mean-square roughness) instead of R_a (arithmetic average).
b: Contact angles listed here refer to those measured at room temperature.
c: Initial contact angle was 66°, but dropped to 36° after 30 minutes.
d: Adhesion reduction factor (*ARF*) is with reference to some control sample. Unless specified otherwise, the control sample used as a reference were bare aluminum specimens.
e: The control sample used as a reference was a smooth *p*-type silicon wafer.
f: The control sample used as a reference was bare steel.

Another trend in ice adhesion literature is to correlate the wettability of the surface to its ice-releasing properties.[17, 36-40] For instance, a well-known paper by Meuler et al.[17] showed that τ_{ice} scales linearly with the practical work of adhesion W_p, or $1 + \cos\theta_R$, where θ_R is the receding water contact angle. A study by Kulinich and Farzaneh[36] demonstrated that while τ_{ice} does not correlate with the sessile contact angle θ, it increases with the contact angle hysteresis $\Delta\theta$ of the surface, where $\Delta\theta = \theta_A - \theta_R$ and θ_A is the advancing contact angle. Table 1, however, illustrates that the most superhydrophobic surfaces with $\theta > 150^\circ$ generally exhibit the lowest *ARF*. Thus, it remains unclear as to how the surface wettability influences τ_{ice}, especially on rough surfaces.

In this study, we investigate the ice adhesion strength on three types of materials: i) superhydrophobic laser-inscribed square pillars, ii) stainless steel 316 Dutch-weaved meshes, and iii) multi-walled carbon nanotube (MWCNT)-covered steel meshes. By considering their surface wettability and topography, we draw conclusions on the governing mechanisms behind ice adhesion, which, in turn, provide insight on how to better design ice-shedding surfaces.

2. Experimental Procedure

2.1. Superhydrophobic femtosecond (fs) laser-inscribed square pillars

The pulsed laser used in this work was an amplified Ti:Sapphire laser (Coherent Libra) with a wavelength of 800 nm, pulse duration <100 fs, and a 10 kHz repetition rate. Copper sheets 0.016” thick (99.90% purity, McMaster-Carr) were cut into 1” x 1.5” coupons and mounted onto a three-dimensional linear translation stage actuated by an XPS universal high performance motion/driver controller (Newport Corp.). The desired trajectory of the translation stage was programmed and relayed to the XPS motion controller by the Gol3D software (GBC&S), which also synchronized the XPS controller with a Uniblitz® 25 mm aperture shutter system (Vincent Associates®). The 3-D translation stage manoeuvred the copper coupons under the incident femtosecond (fs) beam pulses at a set velocity of 2 or 4 mm/s and was positioned such that the theoretical $1/e^2$ beam diameter of the Gaussian beam pulses was 39 μm at the machining plane. A variable attenuator comprising of a half-wave plate and a polarizing beam splitter reduced the laser output power of 4 W to the desired processing power of 800 mW (80 μJ pulse energy).

Laser-inscribed square micro-pillars were machined on the copper specimens over an area of 16 x 16 mm^2 by first etching a set of parallel lines, followed by a second set of parallel lines orthogonal to the first. This scan pattern was repeated five times in order to increase the height of the square pillars. After laser treatment, the samples were cleaned with acetone in an ultrasonic bath for 10 minutes in order to remove residual nanoparticle debris. The copper coupons were then placed inside a vessel containing carbon dioxide gas pressurized to 20 psi and heated to 80 ºC. This was done so as to render the surfaces superhydrophobic, as reported by Kietzig et al.[41]

Figure 1 displays a height intensity map of a representative square pillar topography machined on copper, with parameters a, b, and c depicting the peak width, base width, and height of each square pillar. By adjusting the laser processing parameters, four square pillar arrays of varying widths and heights were fabricated and used in this work. The dimensions of these four different square pillar arrays are given in Table 2. The void volume per pillar V_{void} was calculated by modelling each square pillar as a right pyramidal frustum (truncated right pyramid) and is a measure of how much empty space is present between the pillars. Detailed calculations can be found in the accompanying Supporting Information. High magnification scanning electron microscopy (SEM) images of the top and side of a square pillar in Figure 1 reveal the presence of nano-scale structures, which are a common feature of fs-laser surface texturing.[23]

These nano-sized surface features are products of laser-induced periodic surface structures[42] and nanoparticle deposition,[43] which impart dual-scale roughness to the square pillar topography.

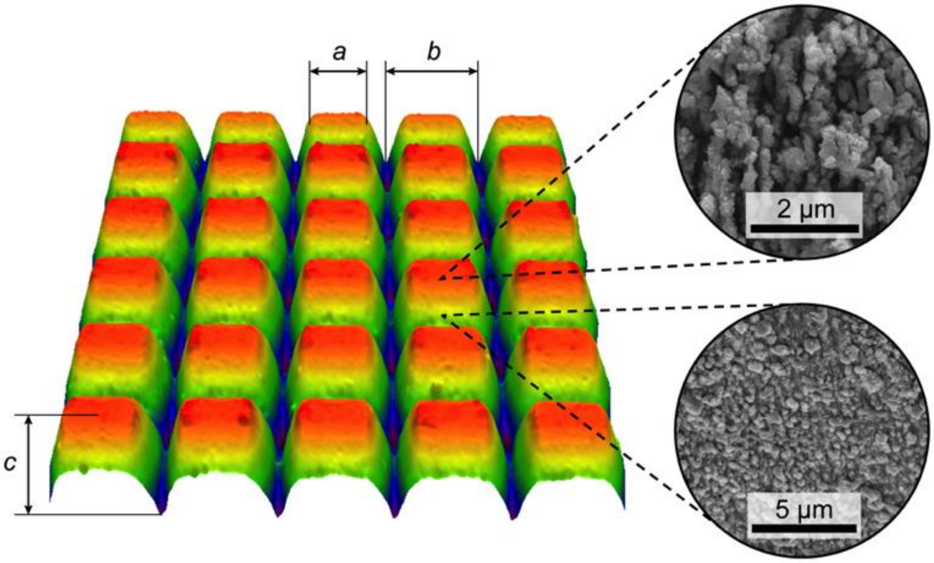

Figure 1. Height intensity map of a laser-inscribed square pillar array on copper obtained using confocal microscopy. High magnification SEM images of the top and side of a square pillar reveal the presence of nanometer-sized features.

Table 2. Peak width (*a*), base width (*b*), and height (*c*) – as depicted in Figure 1 – of the four different laser-inscribed square pillars studied in this work. Samples are listed in order of the void volume per pillar V_{void}. Uncertainties correspond to 95% confidence intervals based on a Student's *t*-distribution with 16 measurements per parameter per sample.

Sample	*a* (µm)	*b* (µm)	*c* (µm)	V_{void} (10^3 µm^3)
1	34.7 ± 1.1	93.2 ± 0.9	59.7 ± 5.3	257 ± 11
2	60.9 ± 2.9	122.7 ± 0.6	60.7 ± 6.5	383 ± 19
3	40.9 ± 2.8	106.5 ± 1.2	94.1 ± 6.5	523 ± 18
4	85.1 ± 3.8	142.0 ± 1.3	93.8 ± 4.5	657 ± 23

2.2. Stainless steel meshes with multi-walled carbon nanotubes

Ultra-fine stainless steel wire cloths, which are typically used for filtration purposes, were purchased from McMaster-Carr. These wire cloths, or meshes, are made from two stainless steel 316 wires of different gauges that are woven together in what is known as a Dutch weave. Figure 2 illustrates the Dutch weave pattern. There are two types of Dutch weaves: twill (Figure 2a) or plain (Figure 2b). For a plain Dutch weave (Figure 2b), thinner wires of diameter d_1 pass over and then under a series of thicker wires in an alternating fashion. The thicker wires with diameter d_2 are also known as warp wires. For the twill Dutch weave configuration (Figure 2a), the thinner wires each pass over and under two warp wires instead of one, which results in a much tighter weave than the plain Dutch weave. Six different wire meshes composed of wires with varying diameters were used in this study; the details of the mesh configurations (wire diameters, wire-to-wire distance, etc.) are listed in Table 3. The pore area A_{pore}, as indicated in Figure 2, was estimated by approximating the smaller wires as a sinusoidal function with a frequency of π/m. The calculation steps, including propagation of uncertainty, are presented in the accompanying Supporting Information.

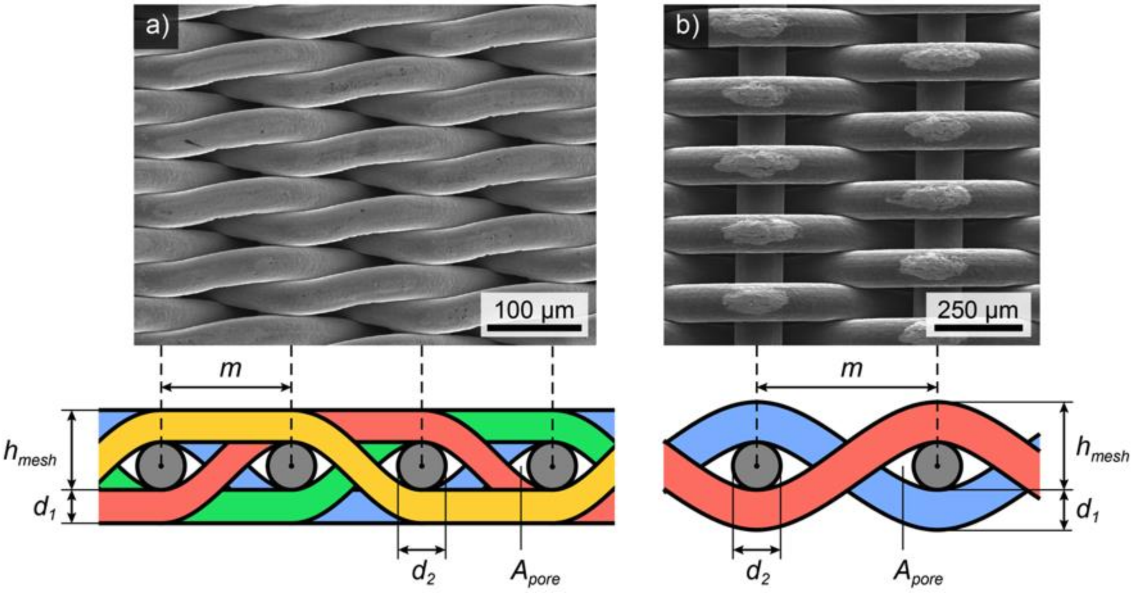

Figure 2. SEM images of stainless steel 316 meshes woven in a) a twill Dutch weave pattern, and b) a plain Dutch weave pattern. The accompanying schematics illustrate in detail how the wires are interwoven and where the pores of the mesh are located.

Table 3. Diameter of wires (d_1 & d_2), warp wire spacing (m), and height (h_{mesh}) of the six different meshes tested in this study, as indicated in Figure 2. The pore size, or area, A_{pore} was estimated by the calculations outlined in the Supporting Information. Uncertainties correspond to 95% confidence intervals based on a Student's t-distribution with 8 measurements per parameter per sample.

Sample	Weave	d_1 (µm)	d_2 (µm)	m (µm)	h_{mesh} (µm)	A_{pore} (µm^2)
1	Twill	22.8 ± 0.5	34.1 ± 1.0	80.0 ± 1.6	23.9 ± 1.1	198 ± 22
2	Twill	39.3 ± 0.8	72.1 ± 3.1	129.3 ± 1.9	37.8 ± 2.1	291 ± 78
3	Twill	50.1 ± 0.7	64.4 ± 0.7	157.6 ± 1.3	74.7 ± 3.5	727 ± 50
4	Twill	37.0 ± 0.5	64.4 ± 0.5	158.6 ± 1.5	49.9 ± 1.1	901 ± 39
5	Plain	109.9 ± 0.6	137.7 ± 1.3	517.9 ± 3.1	193.8 ± 1.8	9003 ± 170
6	Plain	251.5 ± 2.8	350.4 ± 3.2	1072.2 ± 10.1	889.3 ± 45.0	40590 ± 1515

Previous studies have successfully hydrophobized stainless steel meshes by applying coatings and incorporating micro- and nano-scale structures.[44-45] One such technique involves growing multi-walled carbon nanotubes (MWCNT) directly from the stainless steel mesh. Sethi and Dhinojwala[46] fabricated steel substrates coated with carbon nanotubes that exhibited superhydrophobic properties (θ = 167° ± 3°), as well as good electrical conductivity and resilience against harsh environmental conditions. Due to their water repellence, we decided to utilize MWCNT coatings to render the stainless steel meshes superhydrophobic. Furthermore, to the best of the authors' knowledge, there are present no reports in literature that have studied ice adhesion on MWCNT-coated substrates.

Growing MWCNT directly from stainless steel was first demonstrated by Baddour et al.[47] Prior to the growth step, the mesh was cleaned with acetone in an ultrasonic bath for 10 minutes. The stainless steel mesh is then placed at the center of a quartz tube inside a chemical vapour deposition furnace (Linderg-Blue HTF 5500; 120V/30A). The furnace is initially heated up to 700 °C in an inert argon flow of 592 ± 5 sccm. Next, acetylene is injected at 68 ± 5 sccm for 4 minutes. This is followed by an isothermal growth period of 2 minutes under argon flow, after which the system is allowed to cool down. Gas flow rates were monitored and controlled by mass flow controllers (Model 5850E and 01545, Brooks® Instrument). The pressure in the quartz tube remained near atmospheric during the entire process. The MWCNT produced have an average diameter and length of approximately 30 nm and 4 μm, respectively, and form a dense forest on the steel mesh.[48] Figure 3 shows an SEM image of an MWCNT covered steel mesh.

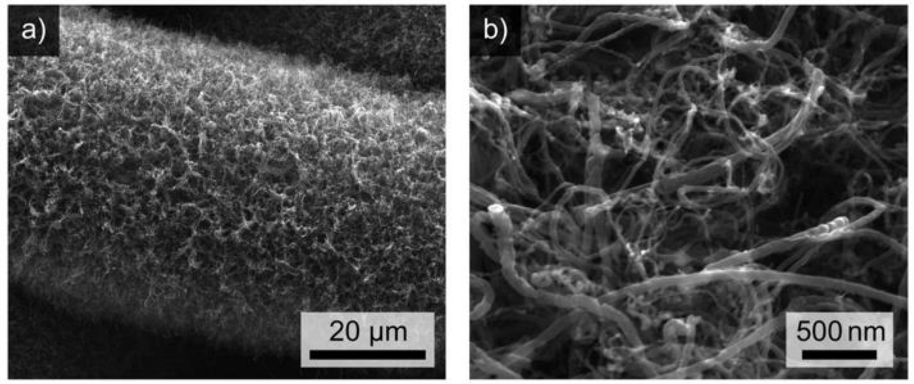

Figure 3. a) SEM image of multi-walled carbon nanotubes (MWCNT) grown from stainless steel 316 meshes. b) Magnified view of individual carbon nanotubes.

2.3. Sample characterization

All the specimens described in the previous sections were imaged in an SEM (FEI Inspect F50) using an accelerating voltage of 5.0 kV and a probe current of approximately 0.1

nA. The geometric dimensions of the samples were measured using 3-D confocal microscopy (Olympus LEXT OLS4000). Measuring the water penetration depth on superhydrophobic surfaces has only recently been made possible through the use of a range of acoustic and imaging techniques.[49-51] In this work, we used a multiphoton laser scanning microscope (Zeiss LSM710) equipped with a 63x water immersion lens (W Plan-APOCHROMAT, Zeiss) to obtain a height intensity profile of the water-air interface. The microscope was operated in reflectance mode using a HeNe Red 633 nm CW laser and a PMT detector.

Water contact angle measurements were performed by a goniometer (DataPhysics OCA 15EC) with reverse osmosis (RO) water that was de-gassed and filtered with a 0.45 µm and 0.2 µm filter. θ_A and θ_R were measured by pumping and withdrawing water from a sessile droplet, respectively, at a rate of 0.05-0.50 µL/s. All room temperature (21 ºC) measurements were repeated 5 times per sample. In order to assess the effect of temperature on θ_A and θ_R, we used a Peltier temperature control chamber (DataPhysics TPC 150) that was liquid-cooled by a refrigerated circulating bath (VWR®) maintained at 20 ºC. The surface temperature was monitored by a Pt 100 thermistor connected to the controller unit. The samples tested – laser-inscribed square pillars and bare stainless steel meshes – were secured to the Peltier plate with aluminum tape to ensure good thermal contact. Before each measurement, we allowed the substrate to equilibrate for 5-7 minutes, and 3 replicates per sample for each temperature were obtained. All contact angle measurements were conducted under 50-60% relative humidity.

2.4. Ice adhesion apparatus

We designed and built a custom adhesion measurement apparatus, depicted in Figure 4, based on previous reports in literature.[17, 29, 34] The specimens were clamped to an air-cooled thermoelectric Peltier cooling unit (CP-200TT, TE Technology Inc.) whose temperature was controlled by a bi-directional temperature controller (TC-36-25 RS232, TE Technology Inc.). We developed a device driver and graphical user interface in *LabVIEW* in order to communicate with the temperature controller. We used a proportional-integral (PI) scheme and tuned the controller using the Ziegler-Nichols method. Two thermistors (MP-3193, TE Technology Inc.) connected directly to the controller, indicated as TT2 and TT3 in Figure 4, monitored the cold and hot sides of the thermoelectric unit, respectively. The temperature of the cold side (TT2) was set to −15 ºC for all experiments and the temperature of the mounted specimen was monitored using a 1/16" T-type thermocouple (TJ36 Series, OMEGA®) attached to a reference sample of the same material (copper or stainless steel 316). The thermoelectric unit was housed within a dedicated aluminum frame (80/20® Inc.) and the upper portion of the apparatus, which would be cooled to sub-zero temperatures, was tightly insulated with polystyrene foam insulation (McMaster-Carr). All experiments were carried out in ambient conditions of 20-22 ºC and 50-60% relative humidity.

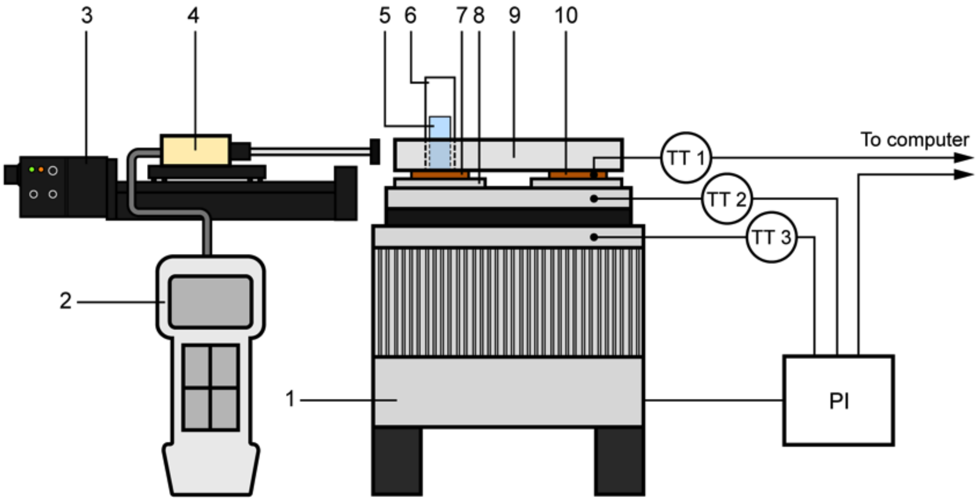

Figure 4. Ice adhesion measurement apparatus. (1) Thermoelectric Peltier cooling unit, (2) digital force gauge, (3) motorized linear translation stage, (4) remote force sensor, (5) water/ice column, (6) glass tube, (7) test specimen, (8) aluminum base plate, (9) aluminum clamp, (10)

reference sample for temperature monitoring. TT = temperature transmitter, and PI = proportional-integral controller.

Each experiment was carried out as follows. A 2.4 ± 0.15 mm thick borosilicate glass tube (custom-made by Pegasus® Industrial Specialties Inc.) with an outer diameter of 15.9 ± 0.20 mm and a height of 50 mm was carefully placed onto the specimen to be tested. The Peltier cold plate was then cooled to −15 ºC, after which 0.5 mL of cooled RO water (5-10 ºC) was gently pipetted into the glass tube and allowed to freeze. After the initial 0.5 mL of water froze, we pipetted another 1.5 mL of water into the glass tube, to a total volume of 2.0 mL. This was done so as to prevent leakage of water from beneath the tube due to hydrostatic pressure. The remaining water was left to freeze completely over approximately 2 hours.

The adhesion strength of ice was evaluated as the shear stress required to dislodge the ice column from the sample surface. A remote force sensor (ZPS-DPU-22, Imada Inc.) mounted onto a linear translation stage (Zaber Technologies Inc.) was driven into the ice column at 0.5 mm/s. The height of the translation stage was adjusted such that the base of the force probe would be no more than 1.5 mm above the specimen surface in order to minimize torque. To obtain the ice adhesion stress τ_{ice}, the peak force measured was normalized over the cross-sectional area of the ice column. After the ice column was dislodged from the substrate, we visually examined its base to assess whether the fracture was adhesive (ice-substrate fracture) or cohesive (ice-ice fracture). Upon the completion of each experiment, the specimens were heated to room temperature and dried for 1-2 hours before the start of another experimental run. Ice adhesion experiments were repeated 4-5 times per sample. Polished copper and stainless steel 316 coupons were used as control specimens.

The temperature of the ice-substrate interface, which will be presented in the Section 4.2, was measured by attaching a fine diameter 0.25 mm J-type thermocouple probe (TJ36 Series, OMEGA®) to the interior of the glass tube. The tip of the thermocouple, which houses the sensing element, was carefully adjusted so that it was flush with the base of the glass tube. We also captured images of the fractured ice surface as follows: upon fracture, the ice column was immediately transferred to an insulated holder and a photograph of the base of the ice column was acquired using a Canon EOS 60D DSLR camera (18.0 Megapixel CMOS sensor) equipped with a Canon MP-E 65 mm f/2.8 1-5x macro lens.

3. Results

3.1. Ice adhesion on superhydrophobic square pillars surfaces

Table 4 summarizes the measurements of θ_A, θ_R, and $\Delta\theta$ on the four different laser-inscribed square pillar topographies, along with values for polished copper. The results indicate that all four square pillar topographies are superhydrophobic since both θ_A and θ_R are located in the vicinity of 150º and $\Delta\theta < 10^{\circ}$. Despite their water repellence, however, the adhesion strength of ice to the laser-textured surfaces is significantly higher than that of polished copper, as shown in Table 4. Thus, $ARF < 1$ for all four samples, and the adhesion of ice increases by up to 67% relative to the polished copper surface. Furthermore, all the shear tests resulted in cohesive fracture, meaning that the fracture occurred within the ice and not at the ice-substrate interface. Fragments from the ice column would remain adhered to the substrate even when the ice column was removed. The plot of τ_{ice} against V_{void} in Figure 5 demonstrates that there is no statistically significant correlation between the two variables. This is expected since the fracture is cohesive and thus τ_{ice} is a measure of the tensile strength of ice rather than the strength of the interface.

Table 4. Summary of contact angle and ice adhesion measurements obtained on superhydrophobic laser-inscribed square pillars fabricated on copper. Uncertainties listed here are 95% confidence intervals based on the Student's *t*-distribution. The control sample used here was polished copper.

Sample	θ_A (°)	θ_R (°)	$\Delta\theta$ (°)	Fracture type	τ (kPa)	*ARF*
Control	96 ± 3	28 ± 4	68 ± 6	Mixed	625 ± 41	-
1	156 ± 2	150 ± 2	7 ± 2	Cohesive	946 ± 189	0.66
2	155 ± 1	147 ± 2	7 ± 2	Cohesive	960 ± 68	0.65
3	155 ± 2	146 ± 3	9 ± 4	Cohesive	1043 ± 176	0.60
4	156 ± 2	148 ± 1	8 ± 1	Cohesive	838 ± 246	0.75

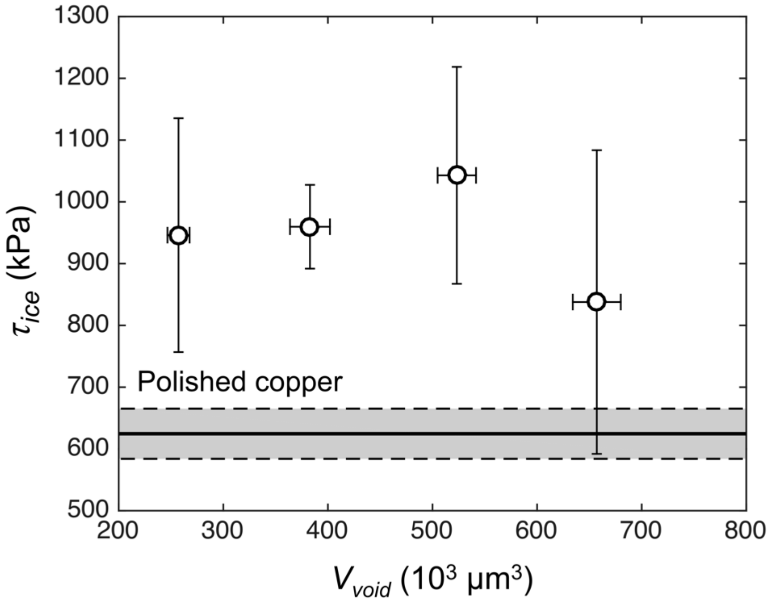

Figure 5. The ice adhesion stress τ_{ice} on superhydrophobic laser-inscribed square pillars is significantly greater than on polished copper and shows no statistical correlation to the void volume per pillar V_{void}. The shaded region corresponds to the 95% confidence interval for $\tau_{control}$ based on the Student's *t*-distribution. Horizontal and vertical error bars correspond to the uncertainties listed in Table 2 and 4, respectively.

3.2. Ice adhesion on bare and MWCNT-covered stainless steel meshes

The dynamic water contact angle measurements on bare and MWCNT-covered stainless steel 316 meshes are listed in Table 5, along with those of polished stainless steel 316. For the bare stainless steel meshes, θ_A increases relative to polished stainless steel while θ_R remains more or less unchanged, except for sample #6 in Table 5. The presence of MWCNT on the mesh wires further increases θ_A, but its effect on θ_R is inconsistent: two meshes (#3 and #5) become superhydrophobic when covered with MWCNT, while θ_R of three MWCNT-covered meshes (#1, #4, and #6) drop dramatically to approximately 0°.

Table 5. Summary of contact angle and ice adhesion measurements obtained on bare and MWCNT-covered stainless steel 316 meshes. Uncertainties listed here are 95% confidence intervals based on the Student's *t*-distribution. The control sample used here was polished stainless steel 316.

Sample	Type	θ_A (°)	θ_R (°)	$\Delta\theta$ (°)	Fracture type	τ (kPa)	*ARF*
Control	-	80 ± 2	15 ± 4	65 ± 4	Mixed	682 ± 46	-
1	Bare	102 ± 6	17 ± 5	85 ± 8	Adhesive	48 ± 15	14.2
	MWCNT	137 ± 17	2 ± 6	135 ± 23	Cohesive	213 ± 18	3.2
2	Bare	109 ± 2	14 ± 4	95 ± 4	Adhesive	89 ± 11	7.7
	MWCNT	156 ± 6	125 ± 15	31 ± 14	Cohesive	121 ± 19	5.6
3	Bare	126 ± 2	18 ± 5	108 ± 6	Adhesive	81 ± 13	8.4
	MWCNT	154 ± 2	144 ± 9	10 ± 11	Cohesive	161 ± 31	4.2
4	Bare	110 ± 7	17 ± 2	93 ± 8	Adhesive	97 ± 20	7.1
	MWCNT	149 ± 3	~ 0	149 ± 3	Cohesive	348 ± 55	2.0
5	Bare	123 ± 2	19 ± 6	104 ± 8	Adhesive	68 ± 11	10.1
	MWCNT	155 ± 1	152 ± 1	3 ± 1	Cohesive	173 ± 25	3.9
6	Bare	108 ± 11	39 ± 9	69 ± 17	Cohesive	298 ± 54	2.3
	MWCNT	117 ± 14	~ 0	117 ± 14	Cohesive	495 ± 27	1.4

The measured ice adhesion stresses are also listed in Table 5. It is immediately obvious that $ARF > 1$ for all the samples listed in Table 5, meaning that the stainless steel meshes reduce the adhesion strength of ice. The highest reduction in adhesion was achieved by the finest bare steel mesh (sample #1 in Table 5) with $ARF = 14.2$, which corresponds to a 93% decrease in adhesion. Another key observation from Table 5 is the fact that for all bare steel meshes except #6, the fracture was adhesive, i.e. the fracture occurred along the ice-steel mesh interface. On the other hand, all MWCNT-covered meshes exhibited cohesive fracture, which occurred in any or all of three ways: i) the carbon nanotubes were stripped from the steel mesh (MWCNT-steel fracture), ii) individual nanotubes were torn apart (MWCNT-MWCNT fracture), or iii) the fracture occurred within the bulk ice phase (ice-ice fracture).

Figure 6 illustrates how τ_{ice} varies with A_{pore} on both bare and MWCNT-covered stainless steel 316 meshes. Here we observe that, for each mesh tested, the MWCNT-covered meshes consistently exhibit a larger τ_{ice} than the bare meshes. Furthermore, it is evident that τ_{ice} on bare meshes increases appreciably after some threshold A_{pore} between 9003 ± 170 and 40590 ± 1515 μm^2. Prior to this threshold, the ice adhesion strength on finer bare meshes (smaller A_{pore}) lies within the range of 48-97 kPa ($7.1 < ARF < 14.2$). However, drawing conclusions on how τ_{ice} is influenced by A_{pore} for MWCNT-covered meshes based on the information given in Table 5 and Figure 6 is not possible since τ_{ice} fluctuates appreciably.

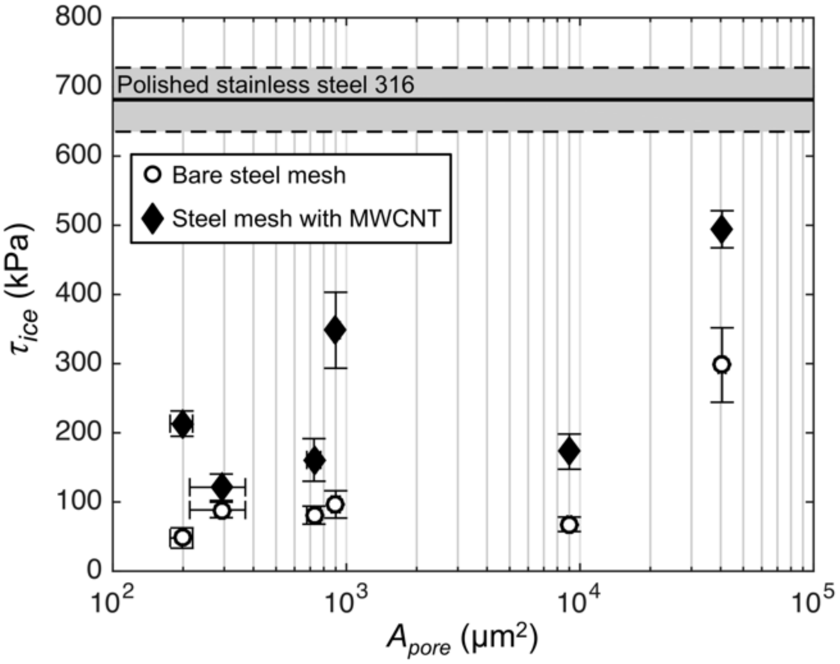

Figure 6. Semi-log plot of τ_{ice} against A_{pore} on both bare and MWCNT-covered stainless steel 316 meshes. The shaded region corresponds to the 95% confidence interval for $\tau_{control}$ based on the Student's *t*-distribution. Horizontal and vertical error bars correspond to the uncertainties listed in Table 3 and 5, respectively.

4. Discussion

The results shown in the previous section provide insight into the governing mechanisms behind ice adhesion to a surface. Section 4.1 first analyzes the effect of wettability on ice adhesion, followed by Section 4.2, which examines the influence of surface topography on ice adhesion.

4.1. Wettability and ice adhesion

Many studies have examined the relationship between wettability and ice adhesion.[13, 17, 29-32, 36-39] For a water droplet wetting a perfectly smooth and chemically homogeneous solid, the reversible work required to separate the water from the solid is known as the thermodynamic work of adhesion, which is given by the Young-Dupré equation: $W_a = \gamma_{LV}(1 + \cos\theta_Y)$, where γ_{LV}

is the liquid-vapour surface tension and θ_Y is the equilibrium, or Young's contact angle. Gao and McCarthy[52-53] modified this equation to describe tensile hydrophobicity as $W_a = \gamma_{LV}(1 + \cos\theta_R)$, which Meuler et al.[17] later designated as the practical work of adhesion W_p. W_p refers to the actual work required to remove a liquid from a non-ideal solid and, for the same liquid, is governed by θ_R only. Meuler et al.,[17] then later Susoff et al.,[18] successfully demonstrated that τ_{ice} scales linearly with the factor $(1 + \cos\theta_R)$, thus strengthening the fact that liquid water-solid adhesion is reflective of ice-solid adhesion.

We plotted the values of τ_{ice} obtained in this study against $(1 + \cos\theta_R)$ in Figure 7 and found no discernible correlation. The lowest τ_{ice} occurs at high $(1 + \cos\theta_R)$, or low θ_R, while the largest τ_{ice} is found at low $(1 + \cos\theta_R)$, or high θ_R. In other words, water-repellent surfaces (high θ_R) exhibited high ice adhesion while the lowest ice adhesion was found on surfaces upon which water readily wet (low θ_R); this is in direct contradiction to what Meuler et al.[17] observed. Furthermore, we see from Figure 7 that adhesive fracture events are confined to low values of θ_R and are associated with low τ_{ice}. On the other hand, cohesive fracture can occur for both large and small values of θ_R and can result in a large range of τ_{ice}, depending on whether the fracture occurs at the MWCNT-steel interface or within the bulk ice, the latter of which yields a high τ_{ice}. Therefore, it is clear from Figure 7 that in our case, τ_{ice} does not scale with the practical work of adhesion.

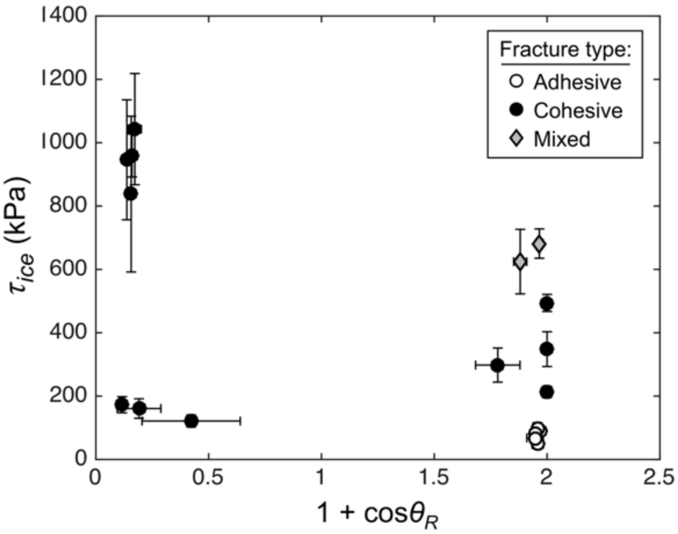

Figure 7. The plot of τ_{ice} against $1 + \cos\theta_R$ shows no discernible correlation and indicates that the ice adhesion stress on the specimens studied in this work does not scale with the practical work of adhesion.

The discrepancy between our work and that of Meuler et al.[17] arises from the fact that while they carried out ice adhesion experiments on relatively smooth surfaces ($R_a < 1$ µm), the samples studied in this work are highly textured with feature sizes on the order of 1 nm to 1 mm (a range spanning 6 orders of magnitude). Evidently, the surface topography of a substrate plays a crucial role in determining the adhesion strength of ice. Since adhesion on smooth surfaces is largely governed by interfacial attractions on the molecular level, water-solid interactions are representative of ice-solid interactions due to the chemical similarities between water and ice.[17] Rough or textured surfaces, on the other hand, introduce an additional complexity for both water and ice adhesion.

When water is deposited on a rough surface, its interaction with the surface falls between two extreme wetting states. The Wenzel, or homogeneous, wetting state refers to the case whereby water fully wets the entire surface and occupies all spaces between surface features. The Cassie, or heterogeneous, wetting state, on the other hand, occurs when water is unable to infiltrate between surface asperities and hence remains suspended upon them. This results in a composite interface beneath the water phase since it is in contact with both the solid substrate and air. A droplet in the Wenzel state will lead to an increase in adhesion relative to a smooth surface due to the increase in water-solid contact area, while the converse is true for a droplet in Cassie state.

For an ice-solid system, however, the adhesion strength of ice to a rough surface does not only depend on the ice-substrate contact area. On the one hand, when ice forms and lodges firmly between the surface features, its adhesion strength may increase dramatically due to mechanical interlocking.[9, 21, 28-29, 54] On the other hand, the presence of trapped air or micro-cracks at the ice-substrate interface can induce local stress concentrations, which significantly lower the work required to remove ice from the surface.[9, 40, 55] Furthermore, the manner in which ice forms on the surface also affects how strongly it adheres to the substrate. Therefore, the correlation between wettability and ice adhesion behaviour for rough or textured surfaces is unsuitable because surface topography influences liquid-solid adhesion differently from how it influences ice-solid adhesion.

We proceeded to investigate why the superhydrophobic square pillars exhibited increased ice adhesion (Section 3.1) relative to polished copper by observing how their wettability changed with temperature. Figure 8 clearly demonstrates that both θ_A and θ_R for the laser-inscribed square pillars decrease with decreasing temperature. Between 20 ºC and 0 ºC, θ_A decreases from 154º ± 2º to 127º ± 6º while θ_R drops sharply from 149º ± 5º to 67º ± 9º. Consequently, $\Delta\theta$ increases from 5º ± 6º to 60º ± 13º. Since θ_A, θ_R and $\Delta\theta$ are determined by the three-phase interactions at the contact line and the activation energy barriers to droplet motion, the results in Figure 8 indicate that as the temperature is lowered, the contact line becomes more and more pinned, i.e. the droplet becomes less mobile. Therefore, the laser-inscribed square pillars lose their non-wetting properties at low temperatures.

Similar behaviour on rough superhydrophobic surfaces has been observed in literature,[13, 56-59] and this trend has been attributed to the condensation of water vapour onto and in between surface asperities when the substrate is cooled below the dew point.[60-63] Any water that comes into contact with the substrate will coalesce with the existing condensate droplets, allowing the water to quickly spread in between the surface structures. Recent work by Yeong et al.[59], however, has demonstrated that superhydrophobic substrates in thermal equilibrium with their surroundings are able to retain their non-wetting properties at low temperatures even under high levels of humidity. They also showed that samples cooled under ambient conditions are susceptible to condensation due the difference in air and substrate temperature. Since, in this present work, ice adhesion experiments were performed under ambient conditions, condensation formation on the laser-inscribed pillars did indeed occur, resulting in a loss of non-wetting performance.

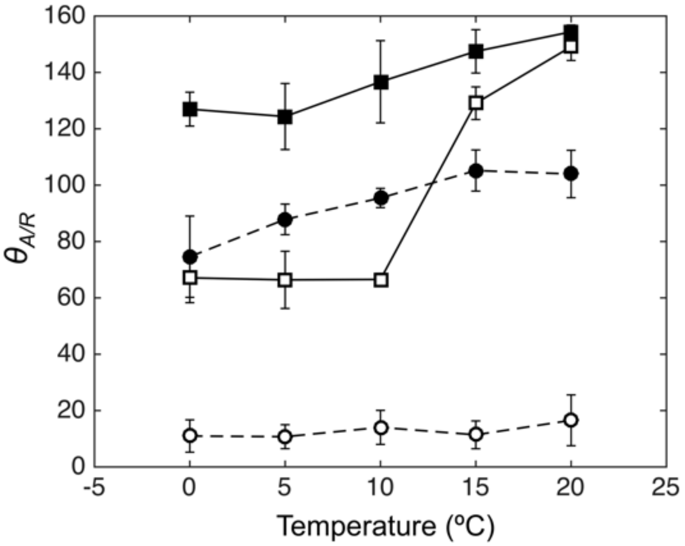

Figure 8. Dependence of advancing (θ_A, filled markers) and receding (θ_R, unfilled markers) contact angles on temperature for superhydrophobic laser-inscribed square pillars (square markers) and bare stainless steel meshes (circular markers). The specimens shown here correspond to samples #3 and #1 in Tables 2 and 3, respectively.

Depending on the surface topography and environmental conditions, a full Cassie-to-Wenzel transition may not occur even from a large temperature drop. In the absence of a complete transition, the surface features are partially wet and the water meniscus sags between the surface structures to a certain position, known as the penetration depth h, which characterizes the degree of water penetration inside the surface roughness.[27] Systems for which $h > 0$ are called metastable Cassie states.[64] As described in Section 2.3, we imaged the water-air and water-solid interfaces of a droplet in contact with the superhydrophobic laser-inscribed square pillars using a confocal microscope equipped with a water immersion lens. The schematic in Figure 9a depicts the shape of the composite water interface suspended on the tops of four square pillars. Here, water wets the textured surface in a metastable Cassie state since the water-air interface sags beneath the tops of the pillars.

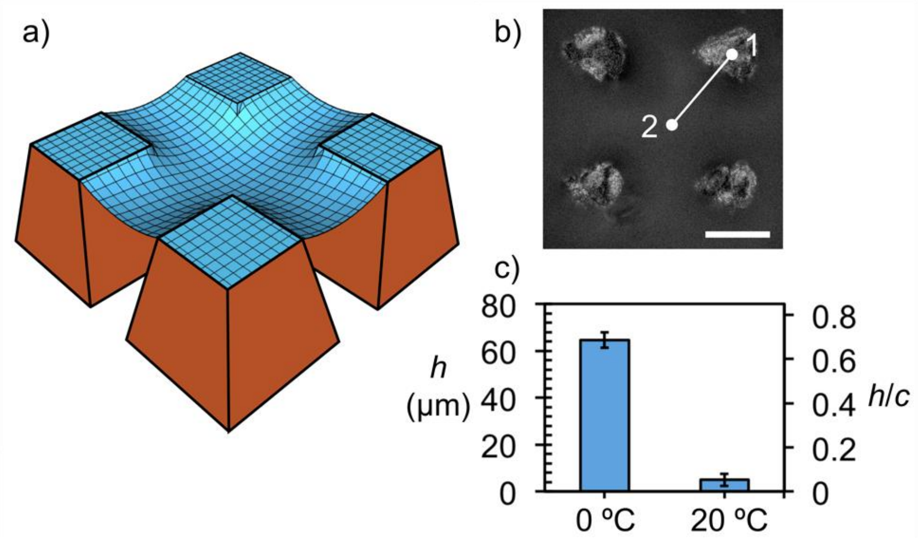

Figure 9. a) Schematic depicting the water-solid and water-liquid interfaces of water wetting square pillars in a metastable Cassie state. b) Grayscale intensity image of the composite water interface obtained using a confocal microscope equipped with an immersion lens at room temperature. The penetration depth *h* was measured as the height difference between points 1 and 2. The scale bar corresponds to 50 µm. c) Measurements of *h* at 0 ºC and 20 ºC illustrate significant water penetration at lower temperature. *h*/*c* refers to the ratio of water penetration depth to pillar height. The specimen studied was sample #3 in Table 2.

The penetration depth is measured as the difference between the top of the pillars and the lowest point of the water-air interface, which is located at the midpoint of the four pillars. This is indicated as points 1 and 2 in Figure 9b, respectively. Figure 9b presents a confocal image of the composite water interface on a square pillar topography (sample #3 in Table 2) at room temperature. A small upper portion of the four square pillars is clearly visible, which indicates that they are being wet by the water phase, while the remainder of the square pillars below – the non-wetted portions – are obscured by the water-air interface. The values of *h* at 20 ºC and 0 ºC are shown in Figure 9c to be 4.9 ± 2.6 µm and 64.6 ± 3.3 µm respectively. Put differently, this means that at 20 ºC, the depth of the water meniscus only descends to 5.2% of the pillar height *c*, but at 0 ºC, the water-air interface drops to 68.7% of the pillar height. Hence, the water-solid contact area is at 0 ºC is significantly higher than at room temperature, resulting in a greater droplet adhesion. As stated previously, the increase in *h* is due to coalescence with condensate droplets that have formed on the sides of the pillars.

We now turn to consider the effect of temperature on the wettability of bare stainless steel meshes. Figure 8 plots the change in θ_A and θ_R for a bare stainless steel 316 mesh (sample #1 in Table 3 specifically), and the results show that while θ_A decreases from 104º ± 8º to 75º ±

14º between 20 ºC and 0 ºC, θ_R remains relatively constant at around 11º. A steady and low θ_R over the 0-20 ºC temperature range implies that the movement of the contact line is unaffected by condensation and requires a greater amount of work than for the square pillar topography. We attempted to measure h on the bare steel mesh but were not able to because water readily wet the substrate and there was no discernible air present beneath the water. This shows that a water droplet will spread over and wet the stainless steel mesh in the Wenzel state and produce a large water-solid contact area. Nevertheless, despite water's affinity for the steel meshes, the adhesion strength of ice to its surface was shown to be very low compared to polished stainless steel, achieving a reduction in τ_{ice} of up to 93%.

The preceding discussion has shown how water-solid adhesion and surface wettability are ill-suited in anticipating ice-solid adhesion, particularly on textured surfaces. Numerous other studies agree, having shown that superhydrophobic surfaces either do not provide a significant reduction in ice adhesion[15, 19, 21, 28, 54] or become damaged after repeated icing/de-icing cycles and eventually lose their ice-releasing properties.[13, 20, 29-31] The alternative, then, is to consider the events that occur at the ice-solid interface during ice formation and ice fracture in order to determine how surface topography influences ice adhesion, and with that, to develop new approaches to design ice-shedding materials.

4.2. Surface topography and ice adhesion

As we have alluded to in Section 4.1, surface roughening or texturing provokes a substantial change in ice adhesion strength as a result of two opposing mechanisms.[9, 55] An increase in adhesion is observed if ice fills the roughness cavities and thus forms a tight mechanical interlock with the substrate. On the other hand, stress concentrations in the form of micro-cracks, air bubbles, or trapped air can cause a drastic decrease in ice adhesion.

Furthermore, the manner in which the ice-solid interface is created – i.e. how the ice forms on the surface – also affects the strength of interface and therefore τ_{ice} as well.[65-66] We will first consider how τ_{ice} is influenced by surface topography for the superhydrophobic square pillars, followed by a discussion of why the surface topography of the stainless steel meshes causes a large drop in τ_{ice}.

For the superhydrophobic laser-inscribed square pillars, we showed in Figure 9c that the water-air interface penetrates into the voids between the two pillars, which, in turn, increases the water-solid contact area. When the water freezes, it expands and pushes against the square pillars on every side, creating a tight grip on the pillars. Consequently, the strength of the ice-solid interface is augmented due to the mechanical anchoring, and this is manifested in the increase in τ_{ice} relative to polished copper (Figure 5). τ_{ice} also increases because mechanical interlocking introduces additional energy dissipative mechanisms during shear loading.[67]

During fracture, the failure of the ice-substrate interface must occur through crack initiation and crack propagation. For a purely interfacial (adhesive) fracture, the crack path follows the ice-solid interface perfectly. In other words, the crack would need to propagate along the tops and sides of the square pillars in the event of a purely adhesive fracture. We know from Table 4, however, that ice adhesion experiments on all 4 of the square pillar specimens resulted in cohesive fracture within the bulk ice. This indicates that the fracture toughness of the mechanically anchored interface is greater than that of ice since cracks propagate along the path of least resistance.[68] As stated in Section 3.1, τ_{ice} does not show any statistically significant variation with the geometry of the square pillars since all fracture events were cohesive (see Figure 5), meaning that the adhesion stress measured corresponded to the tensile strength of ice rather than the interfacial strength.

Mechanical interlocking, however, cannot account for the substantial decrease in ice adhesion strength observed on the stainless steel meshes. There is evidence that the ice-shedding properties of the steel meshes arises from the build-up of residual stresses and the formation of micro-cracks that act as local stress concentrators along the ice-solid interface. Figure 10 displays an image of the base of the ice column immediately after it was dislodged from a bare stainless steel mesh (#5 from Table 5). The fractured surface of the ice is a crisp imprint of the Dutch weave mesh pattern (Figure 2b) and demonstrates the fact that the fracture occurred adhesively. Therefore, the crack paths followed the ice-solid interface and did not deflect into the bulk ice phase.

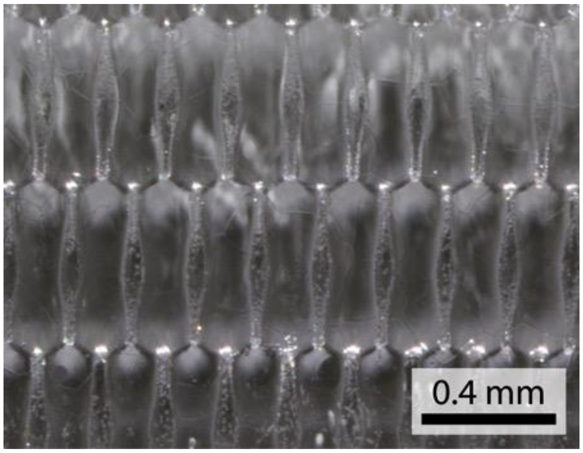

Figure 10. Surface of ice imaged immediately after it was dislodged from a bare stainless steel mesh (sample #5 from Table 3).

We postulate that the decrease in adhesion can be explained by considering the introduction of stress concentrators at the ice-solid interface. The values of θ_R on bare stainless steel meshes lies in the range of 10-40^o, which indicates that the contact line for a droplet deposited on the mesh is strongly pinned to the surface and resists movement. Furthermore, our attempt to image the water-air interface using confocal microscopy (Section 4.1) proved fruitless because water spread over and wet the steel mesh fully. Hence, the water-solid contact area on the steel mesh is greater than for the polished steel control. Upon freezing, water expands, but because of the large water-solid contact area, the ice is unable to accommodate the stress related to the volume expansion. This likely causes the formation of micro-cracks at the ice-solid interface.

In addition, the difference in linear thermal expansion coefficients α_L between ice and stainless steel results in uneven contraction of the two materials during phase change. The linear expansion coefficients of ice[69] and stainless steel 316[70] are $\alpha_{L,ice} = 51 \times 10^{-6}$ K^{-1} and $\alpha_{L,SS} = 18.5 \times 10^{-6}$ K^{-1}, respectively. Figure 11 plots four typical temperature profiles of the water-solid interface T_I after cooled water (5-10 ºC) was pipetted onto the steel mesh. In some instances (red and blue lines), a spike in T_I to approximately 0 ºC was observed due to the release of latent heat from the onset of ice nucleation. The extra energy released due to crystallization raised the temperature of the ice-solid interface, which only returned to the temperature set-point of −15 ºC after 6-8 minutes. In other instances (green and black lines), the phase change occurred immediately after water was deposited onto the surface, so no spike in T_I was observed. Nevertheless, the ice-solid interface still took 6-7 minutes to reach the set-point temperature. Since $\alpha_{L,ice}$ is almost 3 times larger than $\alpha_{L,SS}$, the materials on each side of the ice-solid interface contract at different rates for a ΔT_I of at least 15 ºC over a time period of 6 minutes or more. This discrepancy in α_L produces local strains along the interface and results in the formation of microscopic cracks.

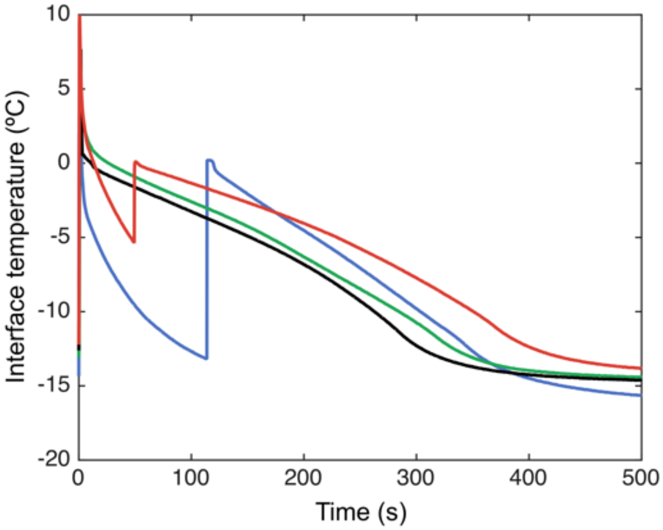

Figure 11. Temperature of the water-solid/ice-solid interface during freezing on a stainless steel mesh (#2 in Table 3). Each line represents a different experimental run. The start of the abscissa corresponds to the time at which the first 0.5 mL of water was pipetted onto the surface of the mesh.

Crack nucleation along the ice-solid interface, caused by the volume expansion during phase change and the mismatch in α_L, act as points of stress concentration when the interface undergoes shear loading. We postulate that the absence of sharp corners on the mesh topography allows interfacial cracks to propagate easily across the ice-solid interface because the crack path does not need to change directions suddenly or drastically. As a result, the fracture occurs adhesively, and the surface of the fractured ice takes on the negative imprint of the steel mesh, as shown in Figure 10. However, we observe in Figure 6 that after a certain mesh pore size between 9003 ± 170 and 40590 ± 1515 μm^2, τ_{ice} increases significantly, and the fracture event becomes cohesive (Table 5). This occurs because the increase in A_{pore} corresponds to an increase in d_1, d_2, m and h_{mesh} (Table 3) compared to the finer meshes. As the mesh becomes coarser, the effect of mechanical interlocking begins to dominate over the effect of interfacial stress concentrations, and this causes crack deflection into the bulk ice, which, in turn, results in a higher τ_{ice}.

Therefore, τ_{ice} is influenced by two competing effects when a surface is roughened or textured. For the superhydrophobic laser-inscribed square pillars, although micro-cracks form at the ice-solid interface due to the phase change, interfacial crack propagation is hindered by the abrupt corners of the square pillars. Thus, instead of following the sudden changes in direction of the ice-solid interface, the crack preferentially deflects into the bulk ice, resulting in cohesive fracture. Mechanical interlocking thus dominates over the effect of local stress concentrators. On the other hand, the gentle undulating topography of the finer bare stainless steel meshes allows preferential crack propagation along the ice-solid interface despite the large ice-solid contact area. Here, the effect of having abundant stress concentrators dominates over mechanical interlocking. However, when the mesh used is too coarse, mechanical interlocking re-dominates, giving rise to an increase in τ_{ice}.

Finally, we address the MWCNT-covered steel meshes. While they exhibited lower τ_{ice} relative to polished stainless steel (*ARF* up to 5.6), the ice adhesion strength on MWCNT-covered meshes was consistently greater than on bare stainless steel. Figure 12 displays SEM images of the MWCNT forest after four icing/de-icing cycles. As seen in Figure 12a, the nanotubes that were previously attached to the stainless steel wire were stripped away, exposing the bare stainless steel beneath. This is an indication that during freezing, the tips of the carbon nanotubes become embedded within the ice phase and are ripped off of the stainless steel substrate when the ice column is sheared from the mesh. The additional energy expenditure in debonding the MWCNT from the steel wires is reflected in an increase in τ_{ice}. Furthermore, the MWCNT become entangled together and form large clumps, as revealed in Figure 12b. The damage inflicted by the removal of ice suggests that MWCNT-covered steel meshes are not suitable as an ice-shedding material.

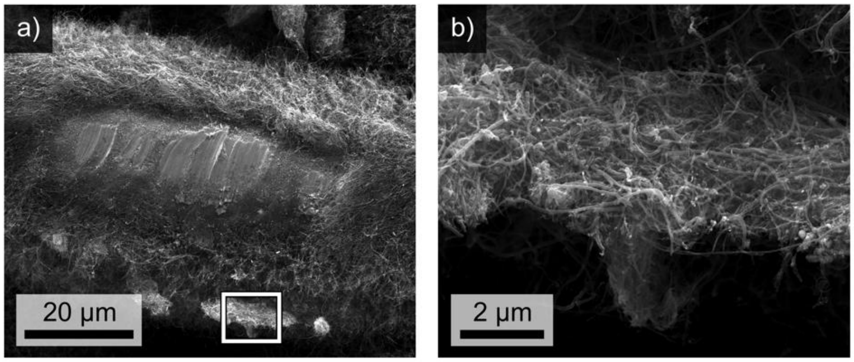

Figure 12. a) SEM image of MWCNT-covered steel mesh after 4 icing/de-icing cycles. The mesh here corresponds to the one shown in Figure 3. b) Magnified view of the indicated area in a).

The results obtained in this study should be placed in context within current literature. The literature cited in Table 1 have *ARF* values ranging from 1.2 to 87.2, and the best performing steel mesh in this work yielded an *ARF* of 14.2. While the steel mesh underperformed the substrates fabricated in other studies,[16, 18-19, 33, 35] its biggest advantage over the materials listed in Table 1 is that it does not need to be treated with any coatings nor infused with any lubricating liquids. Consequently, its cost per unit area is considerably lower than coated ice-shedding materials. In addition, since the steel wires do not possess pointed micro- and nano-scale structures, the steel meshes are durable and can withstand multiple icing/de-icing cycles without sustaining damage. While the data in this work support the use of surface topography towards developing ice-releasing materials, additional research must be carried out to arrive at generalizations for exploiting topography to lower ice adhesion, since the stainless steel meshes in this work only represent a specific case wherein ice adhesion was successfully lowered.

5. Conclusion

In this work, we carried out ice adhesion experiments on three types of surfaces: i) superhydrophobic laser-inscribed square pillars, ii) bare untreated stainless steel 316 meshes, and iii) MWCNT-covered steel meshes. The finest bare steel mesh fared best, reducing the ice adhesion strength by 93% relative to polished stainless steel, while the superhydrophobic square pillars exhibited a significant increase in τ_{ice} relative to polished copper. Surface wettability was found to be a poor predictor of ice adhesion strength because of the different adhesion mechanisms that exist for liquid-solid and ice-solid systems. Instead, we considered how surface topography influences ice adhesion by identifying the two competing effects that arise for a non-planar interface: i) mechanical interlocking and ii) the formation of micro-cracks that act as stress concentrators. On the superhydrophobic square pillars, mechanical interlocking dominates because the ice penetrates between the pillars, anchoring the ice firmly to the surface. On the other hand, the water-ice phase change creates thermal and mechanical stresses at the interface, which result in the formation of micro-cracks that act as interfacial stress concentrators that lower τ_{ice}. Since the mesh topography lacks sharp corners, unobstructed crack growth along the interface can occur, which, in turn, reduces the ice adhesion strength. On the coarsest mesh, however, mechanical interlocking re-dominates and τ_{ice} increases accordingly. The MWCNT-covered steel meshes exhibited τ_{ice} values that were consistently higher than on the bare meshes, and this was attributed to the extra energy expended in tearing the carbon nanotubes from the base mesh.

In conclusion, we have presented for the first time, to the best of our knowledge, a low-cost and durable ice-releasing material that does not require additional coatings or surface treatments. However, the performance of the stainless steel meshes under different icing conditions needs to be further investigated in order to verify its robustness and applicability. Nevertheless, the present work provides greater insight on how surface topography impacts ice adhesion and opens up new ways of designing ice-shedding materials by utilizing their surface topography.

ASSOCIATED CONTENT

Supporting Information. The calculations of V_{void} and A_{pore} can be found in the accompanying file "Supporting Information", along with expressions for the propagation of uncertainty. The following files are available free of charge.

Supporting Information (PDF)

AUTHOR INFORMATION

Corresponding Author

*Tel: +1 (514) 398-1026. E-mail: phillip.servio@mcgill.ca.

Funding Sources

The authors declare no competing financial interests.

ACKNOWLEDGEMENTS

The authors gratefully acknowledge the financial support received from the Natural Sciences and Engineering Research Council of Canada (NSERC) and the Fonds de recherche – Nature et technologies (FRQNT). We would like to thank Dr. Mohammad Jahazi from l'École de technologie supérieure (ÉTS) for the use of their 3D confocal microscope. We would also like to thank Dr. Erika Tse-Luen Wee from the Advanced BioImaging Facility (ABIF) of McGill

University for the use of the multiphoton laser scanning microscope. Finally, we are grateful to the McGill Plasma Processing Laboratory (PPL) for MWCNT synthesis on the stainless steel meshes using their chemical vapour deposition (CVD) reactors.

7. References

1. Ryerson, C. C., Ice Protection of Offshore Platforms. *Cold Reg. Sci. Technol.* **2011,** *65*, 97-110.

2. Dan, H.-C.; He, L.-H.; Zou, J.-F.; Zhao, L.-H.; Bai, S.-Y., Laboratory Study on the Adhesive Properties of Ice to the Asphalt Pavement of Highway. *Cold Reg. Sci. Technol.* **2014,** *104–105*, 7-13.

3. Farzaneh, M.; Volat, C.; Leblond, A., Anti-Icing and De-Icing Techniques for Overhead Lines. In *Atmospheric Icing of Power Networks*, Farzaneh, M., Ed. Springer Netherlands: **2008**; Chapter 6, pp 229-268.

4. Thomas, S.; Cassoni, R.; Mac Arthur, C. In *Aircraft Anti-Icing and De-Icing Techniques and Modeling*, 34th AIAA Aerospace Sciences Meeting, Reno, Nevada, Reno, Nevada, **1996**.

5. Habibi, H.; Cheng, L.; Zheng, H.; Kappatos, V.; Selcuk, C.; Gan, T.-H., A Dual De-Icing System for Wind Turbine Blades Combining High-Power Ultrasonic Guided Waves and Low-Frequency Forced Vibrations. *Renewable Energy* **2015,** *83*, 859-870.

6. Carriveau, R.; Edrisy, A.; Cadieux, P.; Mailloux, R., Ice Adhesion Issues in Renewable Energy Infrastructure. *J. Adhes. Sci. Technol.* **2012,** *26* (4-5), 447-461.

7. Tarquini, S.; Antonini, C.; Amirfazli, A.; Marengo, M.; Palacios, J., Investigation of Ice Shedding Properties of Superhydrophobic Coatings on Helicopter Blades. *Cold Reg. Sci. Technol.* **2014,** *100*, 50-58.

8. Ferrick, M. G.; Mulherin, N. D.; Countermarsh, B. A.; Durell, G. D.; Curtis, L. A.; St. Clair, T. L.; Weiser, E. S.; Cano, R. J.; Smith, T. M.; Stevenson, C. G.; Martinez, E. C., Minimization of Ice Adhesion to Space Shuttle Component Surfaces. *J. Adhes. Sci. Technol.* **2012,** *26*, 473-503.

9. Menini, R.; Farzaneh, M., Advanced Icephobic Coatings. *J. Adhes. Sci. Technol.* **2011,** *25*, 971-992.

10. Mishchenko, L.; Hatton, B.; Bahadur, V.; Taylor, J. A.; Krupenkin, T.; Aizenberg, J., Design of Ice-Free Nanostructured Surfaces Based on Repulsion of Impacting Water Droplets. *ACS Nano* **2010,** *4* (12), 7699-7707.

11. Aboud, D. G. K.; Kietzig, A.-M., Splashing Threshold of Oblique Droplet Impacts on Surfaces of Various Wettability. *Langmuir* **2015,** *31* (36), 10100-10111.

12. Jung, S.; Dorrestijin, M.; Raps, D.; Das, A.; Megaridis, C. M.; Poulikakos, D., Are Superhydrophobic Surfaces Best for Icephobicity? *Langmuir* **2011,** *27*, 3059-3066.

13. Wang, Y.; Xue, J.; Wang, Q.; Chen, Q.; Ding, J., Verification of Icephobic/Anti-Icing Properties of a Superhydrophobic Sruface. *ACS Appl. Mater. Interfaces* **2013,** *5*, 3370-3381.

14. Alizadeh, A.; Yamada, M.; Li, R.; Shang, W.; Otta, S.; Zhong, S.; Ge, L.; Dhinojwala, A.; Conway, K. R.; Bahadur, V.; Vinciquerra, A. J.; Stephens, B.; Blohm, M. L., Dynamics of Ice Nucleation on Water Repellent Surfaces. *Langmuir* **2012,** *28*, 3180-3186.

15. Guo, P.; Zheng, Y.; Wen, M.; Song, C.; Lin, Y.; Jiang, L., Icephobic/Anti-Icing Properties of Micro/Nanostructured Surfaces. *Advanced Materials* **2012,** *24* (19), 2642-2648.

16. Kim, P.; Wong, T.-S.; Alvarenga, J.; Kreder, M. J.; Adorno-Martinez, W. E.; Aizenberg, J., Liquid-Infused Nanostructured Surfaces with Extreme Anti-Ice and Anti-Frost Performance. *ACS Nano* **2012,** *6* (8), 6569-6577.

17. Meuler, A. J.; Smith, J. D.; Varanasi, K. K.; Mabry, J. M.; McKinley, G. H.; Cohen, R. E., Relationships between Water Wettability and Ice Adhesion. *ACS Appl. Mater. Interfaces* **2010,** *2* (11), 3100-3110.

18. Susoff, M.; Siegmann, K.; Pfaffenroth, C.; Hirayama, M., Evaluation of Icephobic Coatings—Screening of Different Coatings and Influence of Roughness. *Appl. Surf. Sci.* **2013,** *282*, 870-879.

19. Bharathidasan, T.; Kumar, S. V.; Bobji, M. S.; Chakradhar, R. P. S.; Basu, B. J., Effect of Wettability and Surface Roughness on Ice-Adhesion Strength of Hydrophilic, Hydrophobic and Superhydrophobic Surfaces. *Appl. Surf. Sci.* **2014,** *314* (0), 241-250.

20. Kulinich, S. A.; Farhadi, S.; Nose, K.; Du, X. W., Superhydrophobic Surfaces: Are They Really Ice-Repellent? *Langmuir* **2011,** *27* (1), 25-29.

21. He, Y.; Jiang, C.; Cao, X.; Chen, J.; Tian, W.; Yuan, W., Reducing Ice Adhesion by Hierarchical Micro-Nano-Pillars. *Appl. Surf. Sci.* **2014,** *305* (0), 589-595.

22. Ahmmed, K. M. T.; Ling, E. J. Y.; Servio, P.; Kietzig, A.-M., Introducing a New Optimization Tool for Femtosecond Laser-Induced Surface Texturing on Titanium, Stainless Steel, Aluminum and Copper. *Opt. Laser Eng.* **2015,** *66* (0), 258-268.

23. Ahmmed, K.; Grambow, C.; Kietzig, A.-M., Fabrication of Micro/Nano Structures on Metals by Femtosecond Laser Micromachining. *Micromachines* **2014,** *5* (4), 1219-1253.

24. Ghalmi, Z.; Farzaneh, M., Experimental Investigation to Evaluate the Effect of Ptfe Nanostructured Roughness on Ice Adhesion Strength. *Cold Reg. Sci. Technol.* **2015,** *115*, 42-47.

25. Boinovich, L. B.; Emelanenko, A. M., Anti-Icing Potential of Superhydrophobic Coatings. *Mendeleev Commun.* **2013,** *23,* 3-10.

26. Schutzius, T. M.; Jung, S.; Maitra, T.; Eberle, P.; Antonini, C.; Stamatopoulos, C.; Poulikakos, D., Physics of Icing and Rational Design of Surfaces with Extraordinary Icephobicity. *Langmuir* **2015,** *31* (17), 4807-4821.

27. Sarkar, A.; Kietzig, A.-M., Design of a Robust Superhydrophobic Surface: Thermodynamic and Kinetic Analysis. *Soft Matter* **2015,** *11* (10), 1998-2007.

28. Varanasi, K. K.; Deng, T.; Smith, J. D.; Hsu, M.; Bhate, N., Frost Formation and Ice Adhesion on Superhydrophobic Surfaces. *Appl. Phys. Lett.* **2010,** *97* (23), 234102.

29. Chen, J.; Liu, J.; He, M.; Li, K.; Cui, D.; Zhang, Q.; Zeng, X.; Zhang, Y.; Wang, J.; Song, Y., Superhydrophobic Surfaces Cannot Reduce Ice Adhesion. *Appl. Phys. Lett.* **2012,** *101* (11), 111603.

30. Kulinich, S. A.; Farzaneh, M., On Ice-Releasing Properties of Rough Hydrophobic Coatings. *Cold Reg. Sci. Technol.* **2011,** *65* (1), 60-64.

31. Farhadi, S.; Farzaneh, M.; Simard, S., On Stability and Ice-Releasing Performance of Nanostructured Fluoro-Alkylsilane-Based Superhydrophobic Al Alloy 2024 Surfaces. *Int. J. Theor. Appl. Nanotechnol.* **2012,** *1* (1), 38-45.

32. Davis, A.; Yeong, Y. H.; Steele, A.; Bayer, I. S.; Loth, E., Superhydrophobic Nanocomposite Surface Topography and Ice Adhesion. *ACS Appl. Mater. Interfaces* **2014,** *6* (12), 9272-9279.

33. Zhu, L.; Xue, J.; Wang, Y.; Chen, Q.; Ding, J.; Wang, Q., Ice-Phobic Coatings Based on Silicon-Oil-Infused Polydimethylsiloxane. *ACS Appl. Mater. Interfaces* **2013,** *5* (10), 4053-4062.

34. Subramanyam, S. B.; Rykaczewski, K.; Varanasi, K. K., Ice Adhesion on Lubricant-Impregnated Textured Surfaces. *Langmuir* **2013,** *29* (44), 13414-13418.

35. Dou, R.; Chen, J.; Zhang, Y.; Wang, X.; Cui, D.; Song, Y.; Jiang, L.; Wang, J., Anti-Icing Coating with an Aqueous Lubricating Layer. *ACS Appl. Mater. Interfaces* **2014,** *6* (10), 6998-7003.

36. Kulinich, S. A.; Farzaneh, M., How Wetting Hysteresis Influences Ice Adhesion Strength on Superhydrophic Surfaces. *Langmuir* **2009,** *25* (16), 8854-8856.

37. Kulinich, S. A.; Farzaneh, M., Ice Adhesion on Superhydrophobic Surfaces. *Appl. Surf. Sci.* **2009,** *255*, 8153-8157.

38. Dotan, A.; Dodiuk, H.; Laforte, C.; Kenig, S., The Relationship between Water Wetting and Ice Adhesion. *J. Adhes. Sci. Technol.* **2009,** *23*, 1907-1915.

39. Dodiuk, H.; Kenig, S.; Dotan, A., Do Self-Cleaning Surfaces Repel Ice? *J. Adhes. Sci. Technol.* **2012,** *26*, 701-714.

40. Nosonovsky, M.; Hejazi, V., Why Superhydrophobic Surfaces Are Not Always Icephobic. *ACS Nano* **2012,** *6* (10), 8488-8491.

41. Kietzig, A.-M.; Hatzikiriakos, S. G.; Englezos, P., Patterned Superhydrophobic Metallic Surfaces. *Langmuir* **2009,** *25* (8), 4821-4827.

42. Young, J. F.; Preston, J. S.; van Driel, H. M.; Sipe, J. E., Laser-Induced Periodic Surface Structure. Ii. Experiments on Ge, Si, Al, and Brass. *Phys. Rev. B* **1983,** *27* (2), 1155-1172.

43. Ling, E. J. Y.; Saïd, J.; Brodusch, N.; Gauvin, R.; Servio, P.; Kietzig, A.-M., Investigating and Understanding the Effects of Multiple Femtosecond Laser Scans on the Surface Topography of Stainless Steel 304 and Titanium. *Appl. Surf. Sci.* **2015,** *353* (0), 512-521.

44. An, T.; Cho, S. J.; Choi, W.; Kim, J. H.; Lim, S. T.; Lim, G., Preparation of Stable Superhydrophobic Mesh with a Biomimetic Hierarchical Structure. *Soft Matter* **2011,** *7* (21), 9867-9870.

45. Srinivasan, S.; Choi, W.; Park, K.-C.; Chhatre, S. S.; Cohen, R. E.; McKinley, G. H., Drag Reduction for Viscous Laminar Flow on Spray-Coated Non-Wetting Surfaces. *Soft Matter* **2013,** *9* (24), 5691-5702.

46. Sethi, S.; Dhinojwala, A., Superhydrophobic Conductive Carbon Nanotube Coatings for Steel. *Langmuir* **2009,** *25* (8), 4311-4313.

47. Baddour, C. E.; Fadlallah, F.; Nasuhoglu, D.; Mitra, R.; Vandsburger, L.; Meunier, J.-L., A Simple Thermal Cvd Method for Carbon Nanotube Synthesis on Stainless Steel 304 without the Addition of an External Catalyst. *Carbon* **2009,** *47* (1), 313-318.

48. Hordy, N.; Rabilloud, D.; Meunier, J.-L.; Coulombe, S., High Temperature and Long-Term Stability of Carbon Nanotube Nanofluids for Direct Absorption Solar Thermal Collectors. *Solar Energy* **2014,** *105*, 82-90.

49. Haimov, B.; Pechook, S.; Ternyak, O.; Pokroy, B., Shape of Water–Air Interface beneath a Drop on a Superhydrophobic Surface Revealed: Constant Curvature That Approaches Zero. *J. Phys. Chem. C* **2013,** *117* (13), 6658-6663.

50. Antonini, C.; Lee, J. B.; Maitra, T.; Irvine, S.; Derome, D.; Tiwari, M. K.; Carmeliet, J.; Poulikakos, D., Unraveling Wetting Transition through Surface Textures with X-Rays: Liquid Meniscus Penetration Phenomena. *Sci. Rep.* **2014,** *4*, 4055.

51. Dufour, R.; Saad, N.; Carlier, J.; Campistron, P.; Nassar, G.; Toubal, M.; Boukherroub, R.; Senez, V.; Nongaillard, B.; Thomy, V., Acoustic Tracking of Cassie to Wenzel Wetting Transitions. *Langmuir* **2013,** *29* (43), 13129-13134.

52. Gao, L.; McCarthy, T. J., Teflon Is Hydrophilic. Comments on Definitions of Hydrophobic, Shear Versus Tensile Hydrophobicity, and Wettability Characterization. *Langmuir* **2008,** *24* (17), 9183-9188.

53. Gao, L.; McCarthy, T. J., Wetting 101. *Langmuir* **2009,** *25* (24), 14105–14115.

54. Chen, J.; Dou, R.; Cui, D.; Zhang, Q.; Zhang, Y.; Xu, F.; Zhou, X.; Wang, J.; Song, Y.; Jiang, L., Robust Prototypical Anti-Icing Coatings with a Self-Lubricating Liquid Water Layer between Ice and Substrate. *ACS Appl. Mater. Interfaces* **2013,** *5* (10), 4026-4030.

55. Sayward, J. M. *Seeking Low Ice Adhesion*; United States Army, Corps of Engineers, Cold Regions Research and Engineering Laboratory: Hanover, New Hamphshire, U.S.A., **1979**.

56. Yin, L.; Xia, Q.; Xue, J.; Yang, S.; Wang, Q.; Chen, Q., In Situ Investigation of Ice Formation on Surfaces with Representative Wettability. *Appl. Surf. Sci.* **2010,** *256* (22), 6764-6769.

57. Yang, S.; Xia, Q.; Zhu, L.; Xue, J.; Wang, Q.; Chen, Q.-m., Research on the Icephobic Properties of Fluoropolymer-Based Materials. *Appl. Surf. Sci.* **2011,** *257* (11), 4956-4962.

58. Heydari, G.; Thormann, E.; Järn, M.; Tyrode, E.; Claesson, P. M., Hydrophobic Surfaces: Topography Effects on Wetting by Supercooled Water and Freezing Delay. *J. Phys. Chem. C* **2013,** *117* (42), 21752-21762.

59. Yeong, Y. H.; Steele, A.; Loth, E.; Bayer, I.; De Combarieu, G.; Lakeman, C., Temperature and Humidity Effects on Superhydrophobicity of Nanocomposite Coatings. *Appl. Phys. Lett.* **2012,** *100* (5), 053112.

60. Dorrer, C.; Rühe, J., Condensation and Wetting Transitions on Microstructured Ultrahydrophobic Surfaces. *Langmuir* **2007,** *23* (7), 3820-3824.

61. Varanasi, K. K.; Hsu, M.; Bhate, N.; Yang, W.; Deng, T., Spatial Control in the Heterogeneous Nucleation of Water. *Appl. Phys. Lett.* **2009,** *95* (9), 094101.

62. Wier, K. A.; McCarthy, T. J., Condensation on Ultrahydrophobic Surfaces and Its Effect on Droplet Mobility: Ultrahydrophobic Surfaces Are Not Always Water Repellant. *Langmuir* **2006,** *22* (6), 2433-2436.

63. Jung, Y. C.; Bhushan, B., Wetting Behaviour During Evaporation and Condensation of Water Microdroplets on Superhydrophobic Patterned Surfaces. *J. Microsc. (Oxford, U. K.)* **2008,** *229* (1), 127-140.

64. Barbieri, L.; Wagner, E.; Hoffmann, P., Water Wetting Transition Parameters of Perfluorinated Substrates with Periodically Distributed Flat-Top Microscale Obstacles. *Langmuir* **2007,** *23* (4), 1723-1734.

65. Raraty, L. E.; Tabor, D., The Adhesion and Strength Properties of Ice. *Proc. R. Soc. London, Ser. A* **1958,** *245* (1241), 184-201.

66. Wei, Y.; Adamson, R. M.; Dempsey, J. P., Ice/Metal Interfaces: Fracture Energy and Fractography. *J. Mater. Sci.* **1996,** *31* (4), 943-947.

67. Kim, W.-S.; Yun, I.-H.; Lee, J.-J.; Jung, H.-T., Evaluation of Mechanical Interlock Effect on Adhesion Strength of Polymer–Metal Interfaces Using Micro-Patterned Surface Topography. *Int. J. Adhes. Adhes.* **2010,** *30* (6), 408-417.

68. Anderson, T. L., *Fracture Mechanics: Fundamentals and Applications*. 2nd ed.; CRC Press, Inc.: Boca Raton, Florida, **1995**.

69. Butkovich, T. R., Thermal Expansion of Ice. *J. Appl. Phys.* **1959,** *30* (3), 350-353.

70. Corruccini, R. J.; Gniewek, J. J., Thermal Expansion of Technical Solids at Low Temperatures. **1961**.

GRAPHICAL ABSTRACT (for Table of Contents)